

3. Impact of annealing temperature on structural and microstructural properties of La₂Zr₂O₇ pyrochlore

3.1 Introduction

Structural defects and microstructure of the constituting phase are major driving forces in all engineering materials to alter their chemical and physical properties. Therefore, the engineering of structural defects and microstructure is of inevitable interest in research entities and industries for developing materials for multifarious applications. Crystalline ceramics are considered a suitable entrant for high-temperature technological applications [1]. The microstructure and structural defects of crystalline ceramics vary as a function of processing temperature and as well as synthetic techniques, i.e. structural defects, grain size, and grain boundaries diverges. [2]. The alteration of structural defects, grain size, and grain boundaries nourish the pyrochlore oxides (A₂B₂O₇) properties such as thermal, mechanical, optical, piezoelectric, dielectric, electrical conductivity, *etc.* [2–4]. Therefore, being curious from the witness of the literature about the engineering of the structural and microstructural specificities of pyrochlore oxides upon processing temperature. The parameters, i.e., annealing time and temperature-induced structural and microstructural mutations are delineated in present chapter. The synthesis processing and characterizations techniques utilized here have been explained in detail in chapter 2.

3.2 Results and Discussion

3.2.1 Structural analysis: XRD

Fig. 3.1 (a) shows the XRD patterns of La₂Zr₂O₇ (LZO) samples annealed at different temperatures, i.e., 1200 to 1500°C with varying the annealing time. All reflection patterns demonstrate the cubic structure pyrochlore phase, which belongs to the $Fd\bar{3}m$ space group [5]. Using the standard ICDD data (#170450), the reflection patterns were examined and found that the reflection peaks matched well with the reference data file. The prudent evaluation of the reflection patterns of LZO [Fig. 3.1] exhibits that the intensities of the reflection pattern increase with the enhancement of annealing temperature and time. The enhancement in the intensities of reflection pattern as a function of annealing time and temperature may be attributed to the increase of structural ordering of LZO samples, i.e., the crystallinity of the LZO samples enhances with annealing temperature and time [6,7].

Here, it is to be noted that the LZO sample annealed at 1200°C for 24 h exhibits the presence of the (111) diffraction plane [Fig. 3.1 (b)], the presence of the (111) diffraction plane at 1200°C evidently confirms the formation of the pyrochlore phase structure. Further, the intensity of the (111) diffraction plane enhances with extension of annealing duration and annealing temperature.

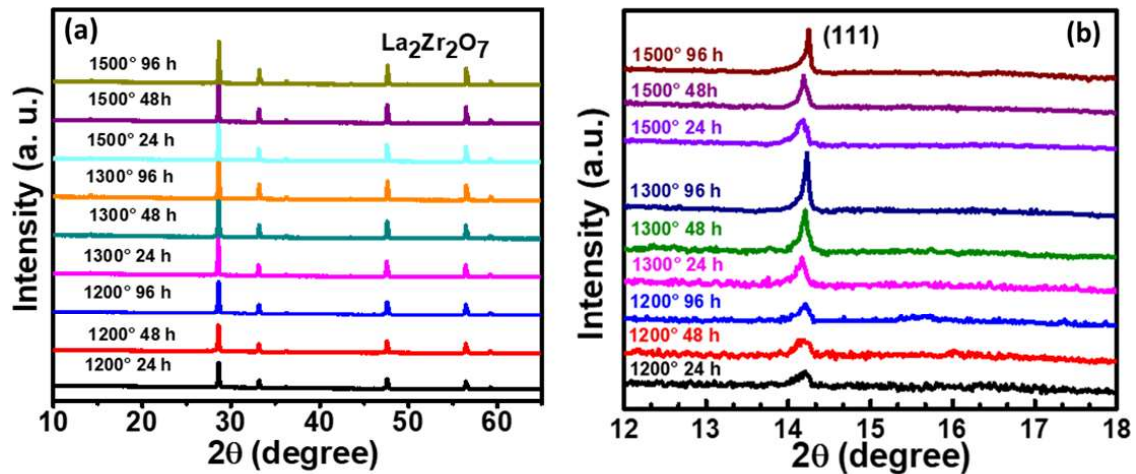


Figure 3.1 Representation of the XRD patterns of LZO (a) and (b) illustrates the magnified view of (111) diffraction plane as a function of annealing temperature and time.

The monotonical enhancement in the intensity of the (111) diffraction plane specifies the augmentation in the degree of ordering of pyrochlore phase with the extension of annealing temperature and time [3][8]. These results suggest that both the parameters, i.e., annealing temperature and time duration play an influential role in engineering the structural ordering of LZO samples. The calculated crystallite size of LZO samples annealed at 1200, 1300, and 1500°C for 96 h are found to be 46 ± 1.8 nm, 69 ± 1.3 nm, and 110 ± 2.0 nm which shown in Fig. 3.2. The crystallite sizes of LZO samples were determined employing the Scherrer equation and it has been explained in section 2.4 of chapter 2.

Fig. 3.2 (a, b) illustrates the variation of crystallite size and lattice strain as function annealing temperature. The crystallite size of LZO samples enhances with the increase of annealing temperature. However, the lattice strain decreases with augmentation of annealing temperature [Fig. 3.2 (b)]. It is reported that the augmentation in grain size and diminution of oxygen defects in the system upon annealing temperature mitigates the grain boundaries stress field and results in, the lattice strain of the system decreasing monotonically as a function of both parameters, i.e., annealing temperature and time [9,10]. Sooraj et al. observed the augmentation of the crystallite sizes with the enhancement of annealing temperature [9]. Similarly, Das et al. reported that the crystallite sizes of $\text{La}_{0.77}\text{Sr}_{0.23}\text{MnO}_3$ NPs monotonically

enhance from 19.0 nm to 243.8 nm with the enhancement of annealing temperature (600 to 1400°C) [10].

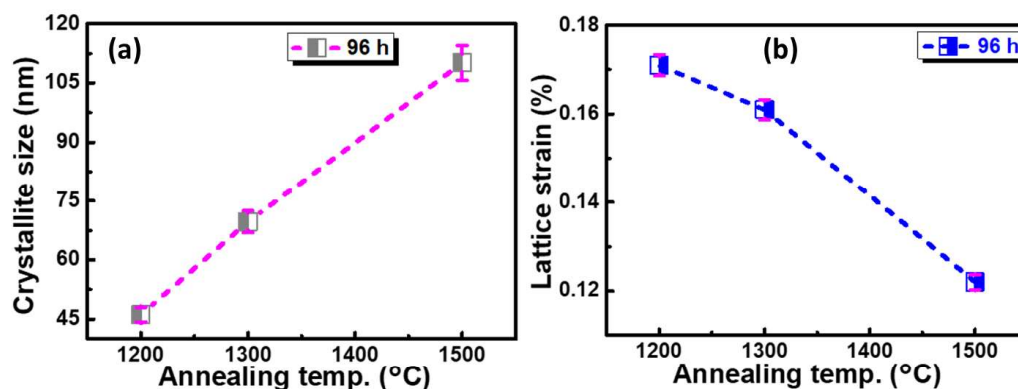


Figure 3.2 Depiction of (a) crystallite size and (b) lattice strain at various annealing temperatures for 96 h.

Chaudhary et al. stated that the lattice strain of CeO₂ oxide NPs decreases monotonically with the augmentation of annealing temperature (200, 600, and 1000°C), i.e., enhancing the crystallite size [11]. Several previous studies accounted for the reduction in the lattice strain with the increase of crystallite size/grain size [11–13].

3.2.1.1 Rietveld Refinement Analysis

Further, to acquire qualitative information about the crystal structure and phase of LZO samples, the Rietveld refinement of the LZO samples has been performed using the Fullprof program [3]. Fig. 3.3 (a-c) exhibits the Rietveld refinement of the LZO samples annealed at three different temperatures, i.e., 1200°C, 1300°C, and 1500°C for 96 h.

During the refinement process, the lattice parameters, occupancies, scale factor, variable atomic coordinate (x_{48f}), and shape parameters were refined. The Pseudo Voigt function was employed to refine the reflection patterns of the LZO samples. The open black circle depicts the observed data, the red line indicates the refined data, the bottom blue color line represents the subtraction of observed and calculated data, and the vertical magenta line illustrates the Bragg's peak positions. We wish to stress that the quality of refining, i.e., “figure of fitting” relies on several factors such as goodness of fit (χ^2), Bragg factor (R_B), weighted profile factor (R_{wp}), and crystallographic factor (R_F), etc.

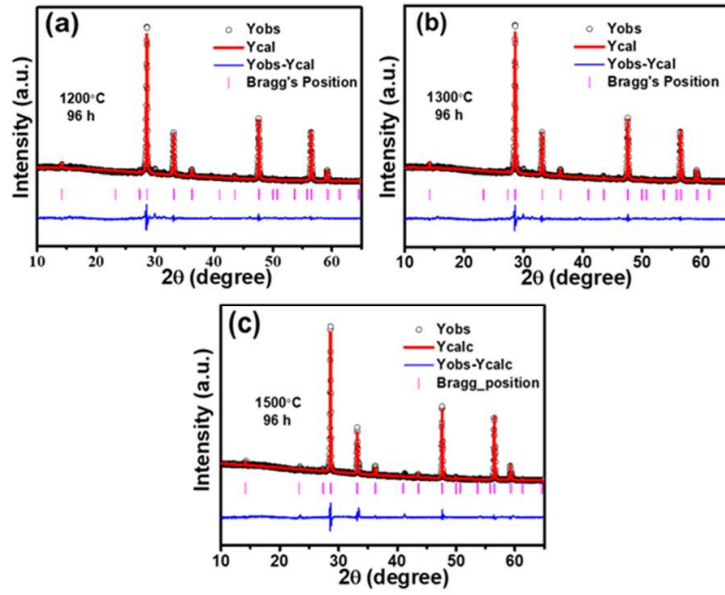


Figure 3.3 Rietveld refinement of the LZO samples annealed at three different temperatures, i.e., 1200°C, 1300°C, and 1500°C for 96 h.

The Rietveld refinement of LZO samples exhibits the presence of superstructure pyrochlore phase [Fig. 3.3 (a-c)] and disregard the existence of the fluorite phase. Table 3.1 exhibits the parameters quantified from the Rietveld analysis of LZO samples and specifies the well refining of LZO samples.

Table 3.1 Depicts the Rietveld refined “figure of merit” parameters (R_B , R_{wp} , R_{exp} , and χ^2).

Sample code	R_B	R_{wp}	R_{exp}	χ^2
1200°C 96h	11.45	17.229	6.901	2.496
1300°C 96h	12.79	19.021	5.845	3.254
1500°C 96h	13.02	18.129	6.172	2.937

Fig. 3.4 (a) illustrates the lattice parameters of LZO samples (evaluated from the Rietveld refinement of corresponding XRD data) and quantified lattice parameters is corroborated with earlier studies[14][15]. It is found that the lattice parameters of the LZO samples decrease with the enhancement of annealing temperature and time duration. The decrement in the lattice parameters is found to be relatively higher for LZO samples annealed at higher temperatures and longer duration. However, the decrement in the lattice parameters is nominal upon annealing at 1200°C for different annealing duration (24, 48, and 96 h). As expected, the X-ray density of LZO samples calculated employing the relation, $\rho_x=8M/N_a a^3$,

enhances monotonically with the augmentation of annealing temperature and time due to diminution in the lattice parameters of LZO samples [Fig. 3.4 (a-b)].

Qin et al. stated that the lattice constant and lattice strain are explicitly correlated to each other [16]. Therefore, we assume that the decrement in the lattice parameters may be associated with reduction of the stress field due to enrichment of crystallite size and decrement of lattice strain [16].

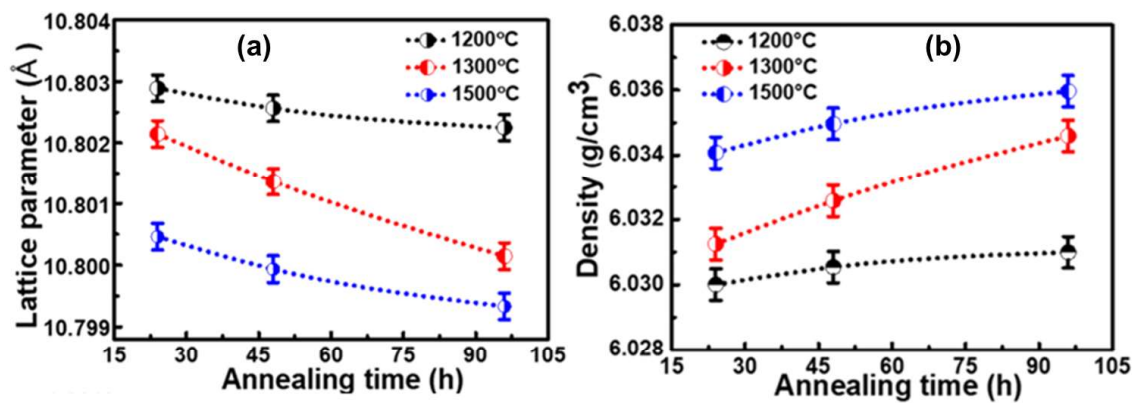


Figure 3.4 Dependence of lattice parameters (a) and (b) X-ray density of LZO samples on annealing temp. and time.

It is noteworthy that the order-disorder structural transition, phase decomposition, and crystalline to amorphous transition in pyrochlore compounds; easily can be achieved via ion irradiation, pressure, and annealing temperature [17]. The pyrochlore compounds are distinctive where order/disordering occur independently in cation and anion sub-lattice via altering the chemical composition and thermal treatment [17]. As we have discussed in the zirconate pyrochlore section in chapter 1, the single variable oxygen parameter, x_{48f} , quantified the structure of pyrochlore systems. As per previous studies [17–19], the values of ‘ x_{48f} ’ for defect fluorite and ordered pyrochlore structure are ~ 0.375 and ~ 0.3125 , respectively. Moreover, the cationic ordering/disordering of compounds can be quantified performing the Rietveld refinement of the XRD patterns of LZO samples because both cations, i.e., La^{3+} and Zr^{4+} possess large variance in the X-ray scattering phenomenon [19].

Fig. 3.5 (a-c) shows the variation of the variable oxygen parameter ‘ x_{48f} ’ and cationic order as a function of annealing temperature and time. It is found that the ‘ x_{48f} ’ decreases monotonically with the enhancement of annealing temperature and time which suggests the enrichment of pyrochlore structure ordering in LZO samples, i.e., the disordering phenomenon in anionic sub-lattice decreased in respect of elevated temperature and time. Further, the order/disordering in the cationic sub-lattice is illustrated in Fig. 3.5 (b-c). Fig. 3.5 (b-c)

confirms that the degree of cation ordering depends on the annealing temperature and time, and enhances with the increase of both the parameters. These results corroborated with the monotonical enhancement in the cationic ordering of $Gd_2Zr_2O_7$ as a function of annealing temperature as reported by Zhang et al. [3]. Therefore, it is inferred that with the augmentation of annealing temperature and time, the structural ordering enhances, thereby increasing the ordering of the pyrochlore structure phase.

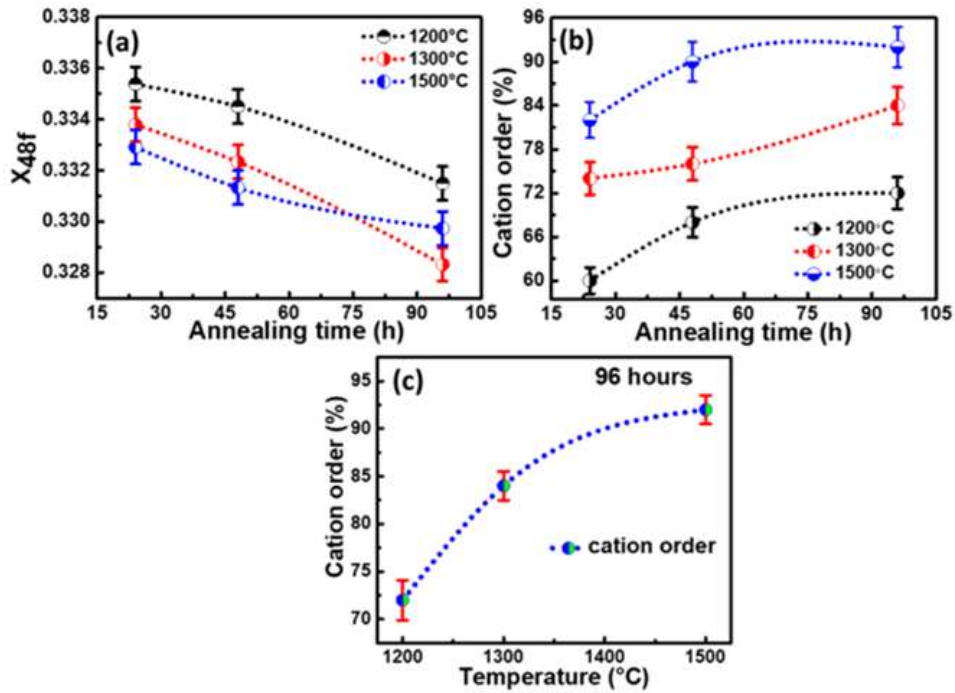


Figure 3.5 Dependence of degree of x_{48f} and cation ordering on annealing temperature and time.

3.2.2 FESEM Analysis

To evaluate the impact of annealing temperature and time on the microstructural properties, we recorded the FE-SEM micrographs of LZO samples. Fig. 3.6 (a-i) exhibits the FE-SEM micrographs of LZO samples annealed at three different temperatures (1200, 1300, and 1500°C) and time (24, 48, and 96 h). The average grain size of LZO samples was determined employing the rectangular intercept process in which the grain size can be defined as.

$$G_t = \sqrt{\frac{4A}{\pi(N_i + N_b/2)}} \quad (3.1)$$

Where, G_t , A , N_i , and N_b express the grain size, area, quantity of grains inside and at the boundaries of a particular area of the rectangle.

It is found that the LZO samples annealed at 1200°C for 24, 48, and 98 h have a grain size of 370 ± 50 , 400 ± 30 , 510 ± 40 nm, which suggest a sluggish grain growth. Similarly, Chaim et al. found a sluggish rate in the evolution of grain growth at low temperatures [20]. Moreover, Fig. 3.6 (a-c) demonstrates that the grain boundaries are not well ascertained which may be associated with the existence of higher porosity. Fig. 3.6 (d-e) exhibits that the evolution of grain size is nominal at 1300°C moving from 24 to 48 h, whereas the grain size is found to be 1150 ± 35 nm for 96 h, which specifies that the evolution of grain is significantly higher for a longer duration. These results suggest that the annealing duration plays a crucial role in the evolution of grain size. Here, it should be noted that the grain sizes and boundaries are well ascertained in the LZO sample (1300°C, 96 h) which may be associated with diminution of the porosity and relatively higher grain growth [Fig. 3.6 (f)].

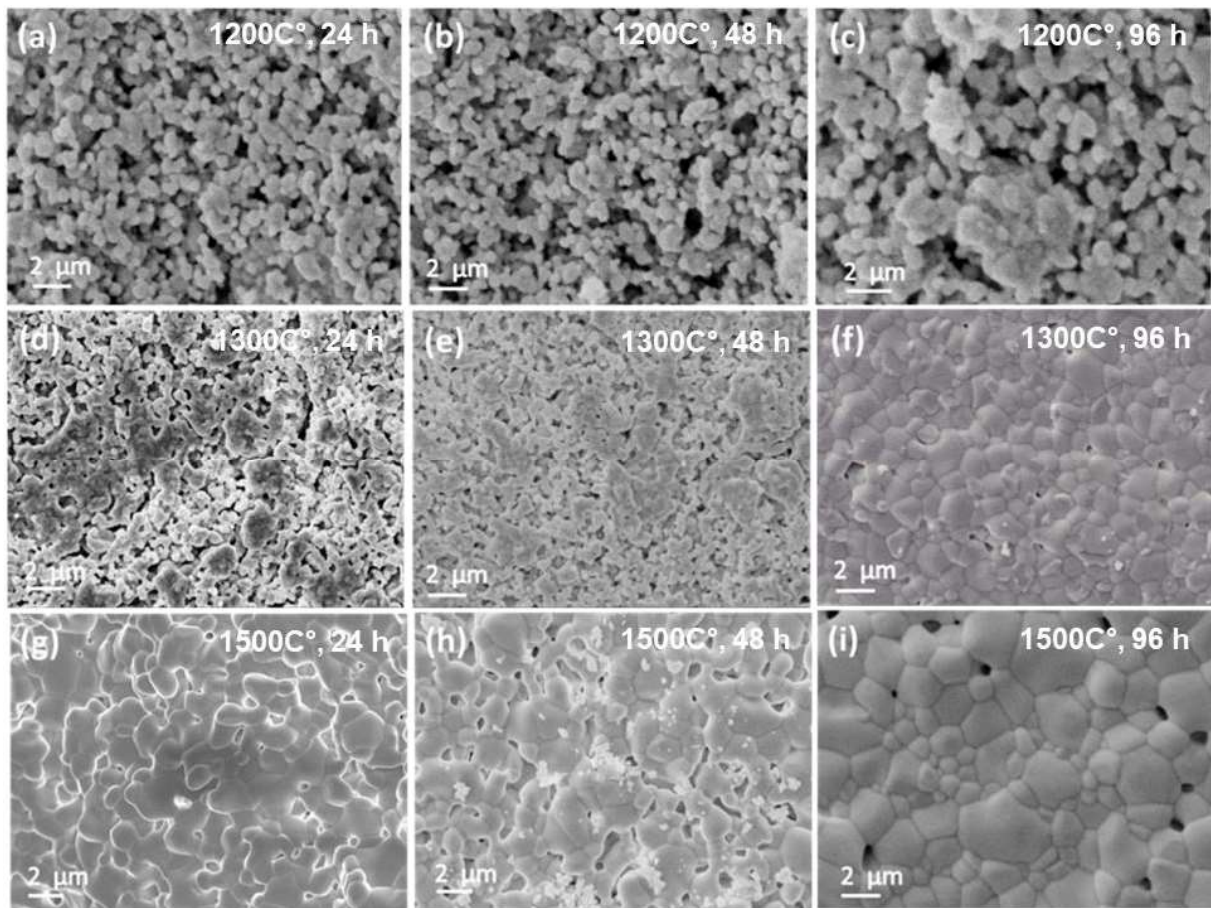


Figure 3.6 FE-SEM micrographs of LZO samples annealed at three different temperatures and times.

Further, analysis of FE-SEM micrographs reveals that the average gain size of LZO samples annealed at 1500°C (24, 48, and 96 h) is relatively higher as compared to corresponding LZO samples annealed at 1200°C and 1300°C (24, 48, and 96 h). Moreover,

Fig. 3.6 (g-i) shows that the grain size enhances monotonically with annealing duration and it is found to be $2.08 \pm 0.30 \mu\text{m}$ for 96 h.

The monotonical enhancement in the grain size of LZO samples with the function of annealing temperature and time [Fig. 3.7 (a)]. Fig. 3.7 (a) suggests that the evolution of grains size is relatively higher at elevated temperature than lower temperature [20]. Earlier, Cobe et al. and Luo et al. investigated the influence of annealing temperature and time on the microstructure. They stated that the evolution of grain size at the elevated annealing temperature for a longer duration is significantly more pronounced than lower annealing temperature for a short duration due to migration of grain boundary and coalition of nano-grains [20–22]. Therefore, in the present study, the migration/diffusion of grain boundaries and coalescence of diminutive grains may be a possible reason for the evolution of grain size and diminution of porosity with the augmentation of annealing temperature and time [20,22].

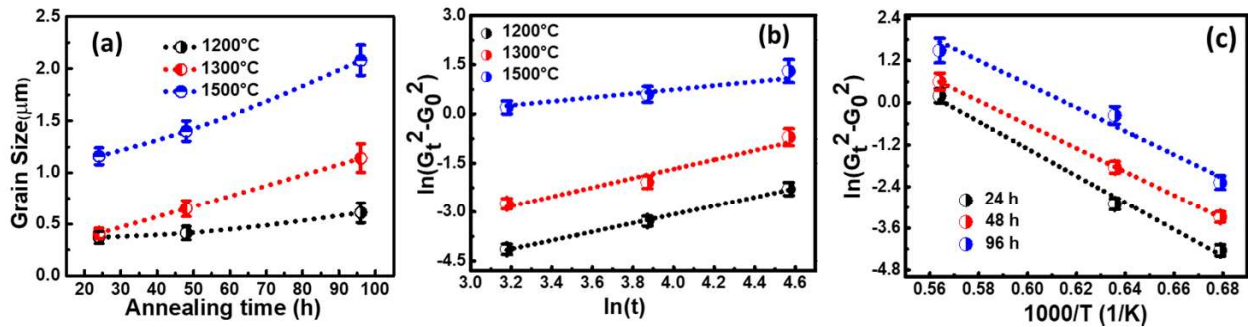


Figure 3.7 Dependence of grain size on annealing temperature and time (a); representation of (b) $\ln(G_t^2 - G_0^2)$ vs $\ln(t)$ and (c) Arrhenius plot.

To understand the role of the annealing time period and temperature on grain growth, the eminent grain growth equation can be described as [20]:

$$G_t^n - G_0^n = k \cdot t \quad (3.2)$$

Where, n represents the grain evolution exponent, and k can be delineated as $k = k_0 \exp(-E_a/RT)$. Further, by simplifying the Eq. (3.2) and including the time exponent ‘ q ’, the Eq. (3.2) can be expressed as.

$$\ln(G_t^n - G_0^n) = \ln(k_0) - \frac{E_a}{RT} + q \ln(t) \quad (3.3)$$

The terms, G_0 and G_t represent the initial grain size and grain size upon annealing at t time; E_a represents the activation energy. The grain growth kinetics exponent in the LZO samples was quantified by plotting the $\ln(G_t^2 - G_0^2)$ vs $\ln(t)$ as shown in Fig. 3.7 (b). It should be noted that the kinetic model of grain growth can be determined using the growth exponent ‘ n ’ and activation energy provides the necessary energy to start the process of crystallization [23]. The

microstructure and growth mechanism are driving forces on which the value of time exponent ‘n’ relies. The different values of ‘n’ represents the different process of controlling the grain growth. On account of time component ‘n’=2, the grain growth phenomenon is influenced by the curvature-driven migration/diffusion of grain boundaries. The grain growth is driven by the volume diffusion if ‘n’ is equal to 3. As shown in Fig. 3.7 (b), the grain growth kinetics equation was fitted considering the $n=2$, which specifies that the grain growth kinetics are influenced by the curvature-driven migration/diffusion of grain boundaries. The value of ‘q’ was determined from the slope of the $\ln (G_t^2 - G_0^2)$ vs $\ln (t)$ and found to be 0.53 ± 0.02 nm which specifies the parabolic dependence on time which is well corroborated with the previous studies [20,24]. Activation energy drives the grain growth and ordering-disordering in the materials [23] and it can be quantified from the slope of the plots of $\ln (G_t^2 - G_0^2)$ vs $1000/T$ [Fig. 3.7 (c)].

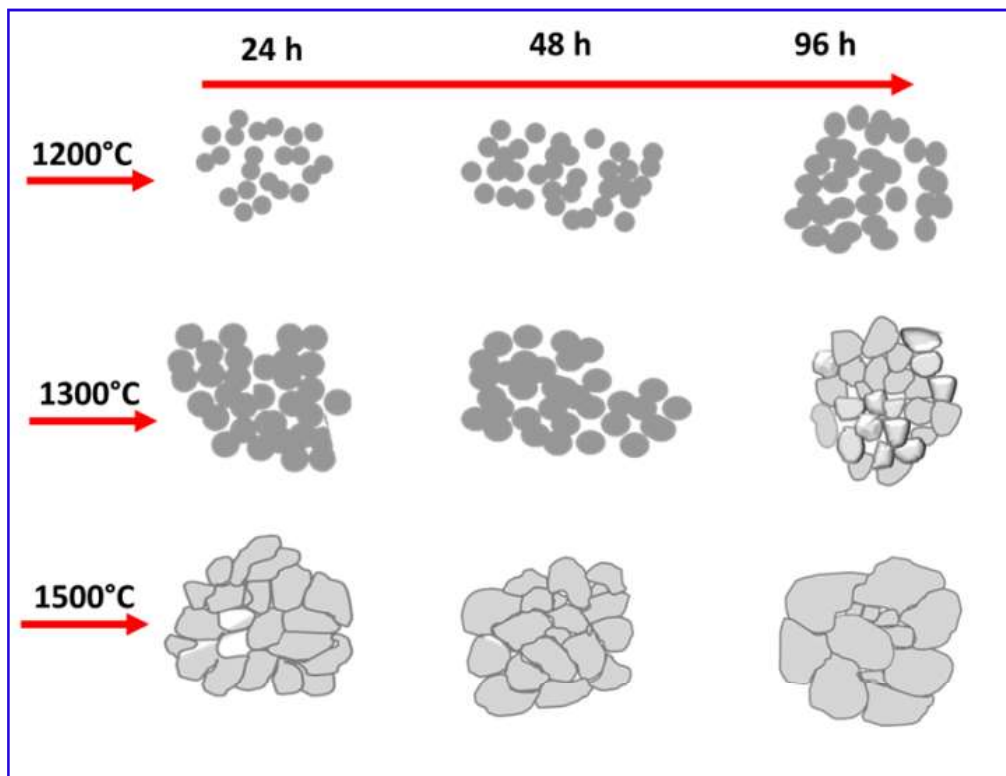


Figure 3.8 Evolution of grain growth of LZO samples as a function of annealing temp. and time.

The activation energy is found to be 590 ± 21 kJ/mol of LZO samples, which corroborated with the activation energy of the yttria-stabilized zirconia [24]. In addition, Chaim et al. found the relatively lower activation energy (546 ± 22 kJ/mol) of the yttria-stabilized zirconia [20]. The curvature-driven migration/diffusion of grain boundaries leads to

the evolution of microstructure [20]. Fig. 3.8 exhibits the evolution of grain growth of LZO samples with the augmentation of the annealing time period and temperature. At the initial phase (1200°C), the migration/diffusion of the grain boundaries in not appear energetic [24], and enrichment in the grain size may be attributed to the coarsening of small grains. The larger size of grain grows due to shrinkage of small grains and grain boundaries moves to reduce the effective area upon annealing of 1300°C for the different duration [25]. The evolution of grain growth are significantly pronounced at higher temperature (1500°C) which specifies that the elevated temperature plays a crucial role in governing the curvature-driven grain growth phenomenon [25]. The curvature-driven grain growth is predominantly governed by the coarsening of remaining small grains and curvature-driven migration/diffusion of grain boundaries [22,24,25].

3.3 Conclusion

In the present study, the structural and microstructural properties of LZO samples were examined with the augmentation of the annealing time period and temperature. The XRD analysis exposed that the crystallinity of the LZO samples enhanced with enrichment of annealing time duration and temperature. The Rietveld refinement of the LZO samples confirmed the formation of cubic structure pyrochlore phase. The qualitative evaluation of variable oxygen parameter ' x_{48f} ' and cation order/disordering revealed the enrichment of the pyrochlore phase structure. FE-SEM results strengthen the XRD studies and established grain growth evolution of LZO samples. The grain growth component revealed that the curvature-driven migration/diffusion of grain boundaries occurred at elevated temperatures for a prolonged duration. An outcome of the investigation divulges that the preselected and destined parameters were found to be capable of tailoring the microstructure and structural ordering that enchant the research community because having tremendous applications in diverse fields.

References

- [1] K.R. Kambale, A. Mahajan, S.P. Butee, Effect of grain size on the properties of ceramics, *Met. Powder Rep.* 74 (2019) 130–136. <https://doi.org/10.1016/j.mprp.2019.04.060>.
- [2] M.A. Subramanian, G. Aravamudan, G.V. Subba Rao, Oxide pyrochlores — A review, *Prog. Solid State Chem.* 15 (1983) 55–143. [https://doi.org/10.1016/00796786\(83\)90001-8](https://doi.org/10.1016/00796786(83)90001-8).
- [3] F.X. Zhang, M. Lang, R.C. Ewing, Atomic disorder in $Gd_2Zr_2O_7$ pyrochlore, *Appl. Phys. Lett.* 106 (2015) 191902. <https://doi.org/10.1063/1.4921268>.
- [4] C. Kaliyaperumal, A. Sankarakumar, T. Paramasivam, Grain size engineering in nanocrystalline $Y_2Zr_2O_7$: A detailed study on the grain size correlated electrical properties, *J. Alloys Compd.* 831 (2020). <https://doi.org/10.1016/j.jallcom.2020.154782>.
- [5] B.C. Chakoumakos, Systematics of the pyrochlore structure type, ideal $A_2B_2X_6Y$, *J. Solid State Chem.* 53 (1984) 120–129. [https://doi.org/10.1016/0022-4596\(84\)90234-2](https://doi.org/10.1016/0022-4596(84)90234-2).
- [6] Y. Kumar, A. Sharma, M.A. Ahmed, S.S. Mali, C.K. Hong, P.M. Shirage, Morphology-controlled synthesis and enhanced energy product (BH) max of $CoFe_2O_4$ nanoparticles, *New J. Chem.* 42 (2018) 15793–15802. <https://doi.org/10.1039/C8NJ02177E>.
- [7] Y. Kumar, P.M. Shirage, Highest coercivity and considerable saturation magnetization of $CoFe_2O_4$ nanoparticles with tunable band gap prepared by thermal decomposition approach, *J. Mater. Sci.* 52 (2017) 4840–4851. <https://doi.org/10.1007/s10853-016-0719-5>.
- [8] L. Kong, I. Karatchevtseva, D.J. Gregg, M.G. Blackford, R. Holmes, G. Triani, $Gd_2Zr_2O_7$ and $Nd_2Zr_2O_7$ pyrochlore prepared by aqueous chemical synthesis, *J. Eur. Ceram. Soc.* 33 (2013) 3273–3285. <https://doi.org/10.1016/j.jeurceramsoc.2013.05.011>.
- [9] S. Sooraj, V.M.S. Muthaiah, P.C. Kang, C.C. Koch, S. Mula, Microstructural evolution and thermal stability of Fe–Zr metastable alloys developed by mechanical alloying followed by annealing, *Philos. Mag.* 96 (2016) 2649–2670. <https://doi.org/10.1080/14786435.2016.1212173>.
- [10] H. Das, A. Inukai, N. Debnath, T. Kawaguchi, N. Sakamoto, S.M. Hoque, H. Aono, K. Shinozaki, H. Suzuki, N. Wakiya, Influence of crystallite size on the magnetic and heat generation properties of $La_{0.77}Sr_{0.23}MnO_3$ nanoparticles for hyperthermia applications, *J. Phys. Chem. Solids.* 112 (2018) 179–184. <https://doi.org/10.1016/j.jpcs.2017.09.030>.

- [11] B. Choudhury, P. Chetri, A. Choudhury, Annealing temperature and oxygen-vacancy-dependent variation of lattice strain, band gap and luminescence properties of CeO₂ nanoparticles, *J. Exp. Nanosci.* 10 (2015) 103–114. <https://doi.org/10.1080/17458080.2013.801566>.
- [12] A. Sharma, Y. Kumar, P.M. Shirage, Structural, optical and excellent humidity sensing behaviour of ZnSnO₃ nanoparticles: effect of annealing, *J. Mater. Sci. Mater. Electron.* 29 (2018) 10769–10783. <https://doi.org/10.1007/s10854-018-9143-8>.
- [13] K. Mazumder, A. Sharma, Y. Kumar, P. Bankar, M.A. More, R. Devan, P.M. Shirage, Enhancement of field electron emission in topological insulator Bi₂Se₃ by Ni doping, *Phys. Chem. Chem. Phys.* 20 (2018) 18429–18435. <https://doi.org/10.1039/C8CP01982G>.
- [14] T. HAGIWARA, K. NOMURA, H. KAGEYAMA, Crystal structure analysis of *Ln₂Zr₂O₇* (*Ln*=Eu and La) with a pyrochlore composition by high-temperature powder X-ray diffraction, *J. Ceram. Soc. Japan.* 125 (2017) 65–70. <https://doi.org/10.2109/jcersj2.16248>.
- [15] K.R. Whittle, L.M.D. Cranswick, S.A.T. Redfern, I.P. Swainson, G.R. Lumpkin, Lanthanum pyrochlores and the effect of yttrium addition in the systems La_{2-x}Y_xZr₂O₇ and La_{2-x}Y_xHf₂O₇, *J. Solid State Chem.* 182 (2009) 442–450. <https://doi.org/10.1016/j.jssc.2008.11.008>.
- [16] W. Qin, T. Nagase, Y. Umakoshi, J.A. Szpunar, Relationship between microstrain and lattice parameter change in nanocrystalline materials, *Philos. Mag. Lett.* 88 (2008) 169–179. <https://doi.org/10.1080/09500830701840155>.
- [17] F.X. Zhang, J.W. Wang, J. Lian, M.K. Lang, U. Becker, R.C. Ewing, Phase stability and pressure dependence of defect formation in Gd₂Ti₂O₇ and Gd₂Zr₂O₇ pyrochlores, *Phys. Rev. Lett.* 100 (2008) 2–5. <https://doi.org/10.1103/PhysRevLett.100.045503>.
- [18] R.C. Ewing, J. Lian, L.M. Wang, Ion beam-induced amorphization of the pyrochlore structure-type: A review, *Mater. Res. Soc. Symp. - Proc.* 792 (2003) 37–48. <https://doi.org/10.1557/proc-792-r2.1>.
- [19] F.X. Zhang, M. Lang, Z. Liu, R.C. Ewing, Pressure-induced disordering and anomalous lattice expansion in La₂Zr₂O₇ pyrochlore, *Phys. Rev. Lett.* 105 (2010) 1–4. <https://doi.org/10.1103/PhysRevLett.105.015503>.
- [20] R. Chaim, Activation energy and grain growth in nanocrystalline Y-TZP ceramics, *Mater. Sci. Eng. A.* 486 (2008) 439–446. <https://doi.org/10.1016/j.msea.2007.09.022>.
- [21] R.L. Coble, Sintering Crystalline Solids. I. Intermediate and Final State Diffusion

- Models, *J. Appl. Phys.* 32 (1961) 787–792. <https://doi.org/10.1063/1.1736107>.
- [22] J. Luo, S. Adak, R. Stevens, Microstructure evolution and grain growth in the sintering of 3Y-TZP ceramics, *J. Mater. Sci.* 33 (1998) 5301–5309. <https://doi.org/10.1023/A:1004481813393>.
- [23] W. Li, L. Chen, Grain growth mechanism and magnetic properties in L1₀-FePt thin films, *AIP Adv.* 7 (2017) 085203. <https://doi.org/10.1063/1.4991423>.
- [24] A.H. Chokshi, Diffusion, diffusion creep and grain growth characteristics of nanocrystalline and fine-grained monoclinic, tetragonal and cubic zirconia, *Scr. Mater.* 48 (2003) 791–796. [https://doi.org/10.1016/S1359-6462\(02\)00519-5](https://doi.org/10.1016/S1359-6462(02)00519-5).
- [25] I.J. Moore, J.I. Taylor, M.W. Tracy, M.G. Burke, E.J. Palmiere, Grain coarsening behaviour of solution annealed Alloy 625 between 600–800 °C, *Mater. Sci. Eng. A.* 682 (2017) 402–409. <https://doi.org/10.1016/j.msea.2016.11.060>.